



# Scaling and spontaneous symmetry restoring of topological defect dynamics in liquid crystal

Yohei Zushi<sup>1</sup> and Kazumasa A. Takeuchi<sup>1</sup>

Edited by Noel Clark, University of Colorado, Boulder, CO; received April 28, 2022; accepted August 24, 2022

Topological defects—locations of local mismatch of order—are a universal concept playing important roles in diverse systems studied in physics and beyond, including the universe, various condensed matter systems, and recently, even life phenomena. Among these, liquid crystal has been a platform for studying topological defects via visualization, yet it has been a challenge to resolve three-dimensional structures of dynamically evolving singular topological defects. Here, we report a direct confocal observation of nematic liquid crystalline defect lines, called disclinations, relaxing from an electrically driven turbulent state. We focus in particular on reconnections, characteristic of such line defects. We find a scaling law for in-plane reconnection events, by which the distance between reconnecting disclinations decreases by the square root of time to the reconnection. Moreover, we show that apparently asymmetric dynamics of reconnecting disclinations is actually symmetric in a comoving frame, in marked contrast to the two-dimensional counterpart whose asymmetry is established. We argue, with experimental supports, that this is because of energetically favorable symmetric twist configurations that disclinations take spontaneously, thanks to the topology that allows for rotation of the winding axis. Our work illustrates a general mechanism of such spontaneous symmetry restoring that may apply beyond liquid crystal, which can take place if topologically distinct asymmetric defects in lower dimensions become homeomorphic in higher dimensions and if the symmetric intermediate is energetically favorable.

liquid crystal | topological defect line | reconnection | scaling law

Topologically nontrivial configurations of order, called topological defects, may appear generically and spontaneously when order is formed. As such, topological defects have been studied in diverse disciplines (1, 2), including cosmology (3), crystals and liquid crystals (2), superconductivity and superfluid (4–9), and biology (10–19) to name but a few. While there exist various kinds of defects characterized by different symmetries and properties, defects may also enjoy common properties across different disciplines. In this context, liquid crystal has the advantage that it is amenable to direct optical observations; various compounds and techniques exist; and as a soft matter system, it shows large response to external fields, being suitable for studying nonequilibrium and nonlinear effects (2, 20). This advantage has been recognized and used for decades, with a notable example of observing liquid crystal defects to test predictions for cosmic strings (21). Moreover, the scope of studies of liquid crystalline defects has been recently extended remarkably, including the use of defects as templates for molecular self-assembly (22) and the recent surge of investigations of active nematic systems bearing relevance to life phenomena (10–19).

Despite this history, resolving fully three-dimensional (3D) structures of liquid crystal defects has not been straightforward, even for the simplest kind of defects, namely nematic disclination lines. Well-known techniques for 3D observation of defects and other orientational structures are fluorescence confocal polarizing microscopy (23, 24) and two- or three-photon excitation fluorescence polarizing microscopy (25–27). Both techniques allow one to reconstruct the 3D structure of the director field, by which one can determine the position and structure of defects in principle. To do so, however, one needs to reduce the effect of defocusing and polarization changes due to the birefringence of liquid crystal. For singular defects, such as nematic disclinations, scattering at the core gives another difficulty. The effect of birefringence can be significantly reduced by partial polymerization of the medium (28), but this cannot be used to study dynamics of defects.

Here, we propose a method to capture dynamically evolving 3D structures of nematic disclination lines by using confocal microscopy and a recently reported accumulation of fluorescent dyes around the singular core of defects (29). This method allows us to visualize the disclinations directly (Fig. 1), without reconstructing and analyzing the director field. Using this technique, we observe reconnections of disclinations—a hallmark of such topological defect lines—and characterize the reconnection dynamics in terms of scaling and symmetry.

## Significance

When order is formed, topological defects may appear generically, and as such, they are a key to characterize and control the order formation observed in different fields of physics and related disciplines. At the heart of such approaches is disentangling universal and nonuniversal aspects of topological defect dynamics. We do so by realizing direct observation of three-dimensional (3D) dynamics of liquid crystalline defects. Analyzing topological rearrangements called reconnections, on one hand, we establish the validity of the scaling law known for quantum fluid and two-dimensional (2D) liquid crystal; on the other hand, we reveal that the asymmetry present in 2D defect dynamics disappears in 3D. This finding is accounted for by a general mechanism that may hold beyond liquid crystal.

Author affiliations: <sup>1</sup>Department of Physics, The University of Tokyo, Tokyo 113-0033, Japan

Author contributions: K.A.T. designed research; Y.Z. performed research; Y.Z. and K.A.T. analyzed data; and Y.Z. and K.A.T. wrote the paper.

The authors declare no competing interest.

This article is a PNAS Direct Submission.

Copyright © 2022 the Author(s). Published by PNAS. This open access article is distributed under Creative Commons Attribution-NonCommercial-NoDerivatives License 4.0 (CC BY-NC-ND).

<sup>1</sup>To whom correspondence may be addressed. Email: kat@kaztake.org.

This article contains supporting information online at <https://www.pnas.org/lookup/suppl/doi:10.1073/pnas.2207349119/-DCSupplemental>.

Published October 3, 2022.

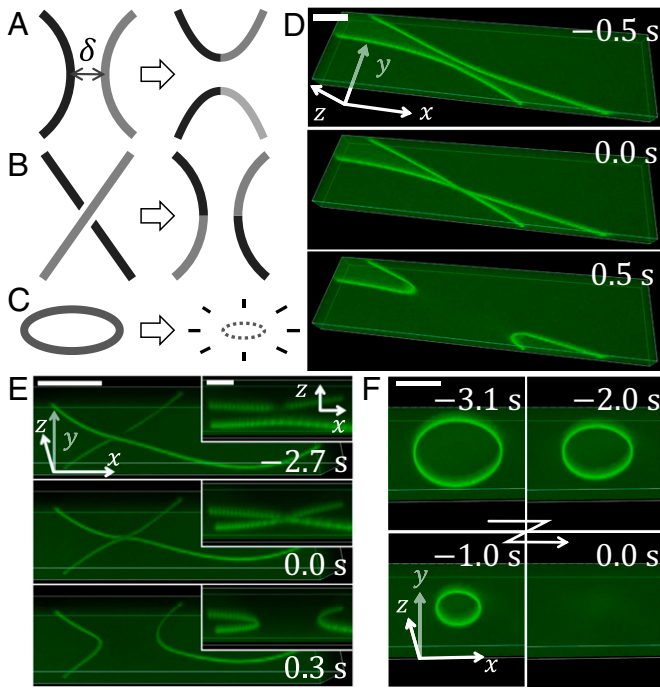


**Fig. 1.** Reconnections and loop shrinkage. (A–C) Sketches of an in-plane reconnection (A), an intersecting reconnection (B), and a loop shrinkage (C). (D–F) Confocal observations of an in-plane reconnection (D), an intersecting reconnection (E), and a loop shrinkage (F) (Movies S1–S4). E, Insets display side views of the event shown in E. (Scale bars: D–F, 50  $\mu\text{m}$ ; E, Insets, 20  $\mu\text{m}$ .)

## Observations of Disclination Dynamics

To study disclination dynamics, we add fluorescent dye to liquid crystal and observe the fluorescence from the dye localized at the 3D disclinations by confocal microscopy. Using the previously reported apparent length scale of dye accumulation,  $\approx 0.33 \mu\text{m}$  (29), and the typical value of the diffusion coefficient of dye molecules,  $\approx 10^{-10} \text{ m}^2/\text{s}$  (24, 30), we evaluate that dye can follow the evolution of disclinations at the time resolution of roughly 1 ms. This is to compare with the timescale of the disclination dynamics, which can be evaluated at  $\gamma_1 \ell^2 / K$  with Frank constant  $K$ , rotational viscosity  $\gamma_1$ , and characteristic length scale  $\ell$  of disclination lines (such as the radius of curvature) (20). For typical mesogens (including the one used in this work), we have  $K \approx 10^1 \text{ pN}$  and  $\gamma_1 \approx 10^2 \text{ mPa} \cdot \text{s}$  (20), so that, for example, disclinations of length scale  $\ell \approx 10^1 \mu\text{m}$  evolve over a timescale of roughly 1 s. Therefore, the disclination dynamics can be faithfully captured by confocal images acquired at a time interval between 1 ms and 1 s (or longer for disclinations of larger length scales). To fulfill this condition, we chose a laser-scanning confocal microscopy equipped with a resonant scanner working at 8 kHz and a piezo objective scanner (Materials and Methods has details).

A liquid crystal sample, MLC-2037 doped with fluorescent dye Coumarin 545T and electrolyte tetra-*n*-butylammonium bromide, was filled in a cell that consists of parallel glass plates with transparent electrodes (indium tin oxide) separated by 130  $\mu\text{m}$ -thick spacers (Materials and Methods). The planer alignment condition was imposed on the cell surfaces. We generated a large density of disclinations by using an electrohydrodynamic turbulence (20), induced by an electric field applied to the liquid crystal sample. The electric field was then removed, and disclinations started to undergo relaxation. We indeed observed a large density of singular disclinations upon removal of the electric field. The disclinations then

exhibited coarsening dynamics, including reconnections and loop shrinkage (Fig. 1 and Movies S1–S4), similar to those observed previously by bright-field microscopy (21, 31–34). We also observed nonsingular disclinations terminating at singular ones (SI Appendix, Fig. S1), as well as other kinds of defect structure, as reported in past bright-field studies (31, 32).

Most disclination lines were found near the midplane between the top and bottom surfaces and extended mostly horizontally because of the homogeneous boundary condition we imposed. As a result, most of the observed reconnections were classified into the following two kinds: in-plane reconnections (Fig. 1 A and D and Movie S2) and intersecting reconnections (Fig. 1 B and E and Movie S3). An in-plane reconnection consists of a pair of curved disclinations in a nearly single horizontal plane, which approach in that plane and reconnect (Fig. 1 D and Movie S2). An intersecting reconnection consists of a pair of disclinations crossing at different  $z$  positions, which approach vertically and reconnect (Fig. 1 E and Movie S3). In this case, the upper disclination appeared dark above the intersection (Fig. 1 E, Insets) and apparently bent when the pair is close enough, presumably because of the lensing effect due to the lower disclination. Since this prevented quantitative analysis, in the following we focus on the in-plane reconnections and study their reconnection dynamics. We analyzed a total of 40 in-plane reconnections without any noticeable nonsingular disclinations in the field of view.

## Scaling Law for In-Plane Reconnections

Using the confocal images of the in-plane reconnections, we extracted the 3D positions of the two disclinations until the moment of the reconnection (Materials and Methods). Measuring how the minimum distance between the two disclinations,  $\delta(t)$ , decreases with time  $t$  (Fig. 2), we found the following scaling law for all in-plane reconnections:

$$\delta(t) \simeq C|t - t_0|^{1/2}, \quad [1]$$

with a coefficient  $C$ . This power law is identical to that for annihilation of point disclinations in two-dimensional (2D) nematics (35, 36) as well as that for reconnections of quantum vortices in quantum fluids (6, 7, 36). It is interesting to note that the interaction of disclinations in 3D nematics was theoretically

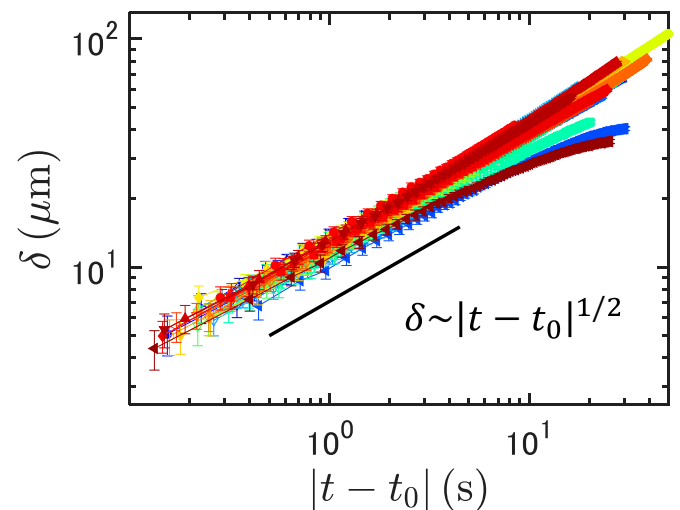


**Fig. 2.** The scaling law for in-plane reconnections. Results for all 40 reconnection events are shown with different colors. The error bars indicate the uncertainty evaluated from the slicing and the Gaussian fitting used to determine the coordinates of the disclinations (Materials and Methods).

evaluated only very recently (37, 38) and that the power law in Eq. 1 was derived in the case of straight disclinations. Although the experimentally observed disclinations were not straight but curved inward (Fig. 1D), we may argue that the time evolution of  $\delta(t)$  is dominated by the interaction between the two closest points, so that the disclination curvature did not affect the observed power law significantly. The scaling law (Eq. 1) was also observed numerically for curved disclinations in ref. 38. Of course, it is important to extend those theoretical approaches to the case of curved disclinations and confirm the robustness of the power law in Eq. 1.

### Apparent Asymmetry in the Laboratory Frame

In the case of 2D nematics, disclinations are point like and characterized by a topological invariant called the winding number. Energetically stable are the disclinations of winding number  $\pm 1/2$  (see the sketches in Fig. 4A), and disclinations of opposite signs attract each other, approach, and annihilate. Here, it is well known that such a pair of  $+1/2$  and  $-1/2$  disclinations approaches in an asymmetric manner, due to the different backflow generated by the two defects (35, 39). It would be then natural to expect analogous asymmetry to arise for line disclinations in 3D nematics. However, this is not so trivial from the viewpoint of topology because  $+1/2$  and  $-1/2$  disclinations are topologically equivalent (homeomorphic) in 3D nematics (1, 2, 20). Besides, unlike point disclinations, line disclinations have shapes and are deformable, giving additional potential sources of asymmetry.

Here, we inspected this asymmetry experimentally. Instead of the distance  $\delta(t)$  between reconnecting disclinations, we measured the distance between each disclination line and the

reconnection point,  $D_1(t)$  and  $D_2(t)$  (Fig. 3A). Plotting  $D_i(t)^2$  against  $t - t_0$ , we found a power law  $D_i(t) \simeq C_i |t - t_0|^{1/2}$  analogous to Eq. 1, with coefficients  $C_i$  that are typically asymmetric between the two disclinations (Fig. 3C has an example). The asymmetry was also clear from the defect motion (SI Appendix, Fig. S2A). Using the coefficients  $C_i$ , we define the asymmetry parameter  $A$  by

$$A \equiv \frac{\max\{C_1, C_2\}}{\min\{C_1, C_2\}} \quad [2]$$

and determined it for each reconnection event. By definition,  $A = 1$  for symmetric reconnections, and  $A > 1$  for asymmetric ones. The histogram of  $A$  (blue bars in Fig. 3D) shows that most in-plane reconnections appear to be significantly asymmetric. We suspected that the different curvature of the two disclination lines may contribute to this asymmetry, but this effect turned out to be minuscule (SI Appendix).

### Disappearance of Asymmetry in the Comoving Frame

Let us now recall the fact that disclinations have extended line structures and also, that the studied pairs were not the only defects present in the system. It is, therefore, reasonable to consider that the reconnection dynamics may be affected by such extrinsic factors, which may induce flow and director changes superimposed to the intrinsic reconnection dynamics. These effects are expected to add a drift to the intrinsic motion of reconnecting disclinations. To evaluate this drift, we located the point on each disclination that was closest to the reconnection point and inspected the motion of the midpoint  $\vec{M}(t)$  of the pair of the closest points (Fig. 3B). If the dynamics of the two disclinations is perfectly symmetric, the motion of this midpoint is the drift itself and will not show any singularity near the reconnection time. If the dynamics is not symmetric, this midpoint will partly include the reconnection dynamics, showing the same singularity as  $D_i(t) \propto |t - t_0|^{1/2}$ . This was indeed confirmed for the case of pair annihilation of 2D point disclinations reported by Tóth et al. (39) (SI Appendix, Fig. S3). For 3D disclination lines, the behavior of  $\vec{M}(t)$  is shown in Fig. 3E, Inset for the pair displayed in Fig. 3C. This clearly shows linear dependence on time, suggesting that the intrinsic dynamics of reconnection is actually symmetric. Moreover, using the drift velocity  $\vec{V}$  evaluated by fitting  $\frac{d\vec{M}}{dt}$ , we define the comoving frame and measure the distance  $\tilde{D}_i(t)$  between the closest point and the reconnection point in this comoving frame. The result shows that, remarkably, the reconnection dynamics in this comoving frame is nearly perfectly symmetric (Fig. 3E and SI Appendix, Fig. S2B). We carried out this analysis for all reconnection events, and for all cases, the asymmetry parameter became very close to one (red bar in Fig. 3D), the largest deviation being  $A = 1.03 \pm 0.01$ . Note that although the asymmetry parameter  $A$  is expected to be independent of the choice of reference frame in the limit  $t \rightarrow t_0$ , it does depend in practice because the limit  $t \rightarrow t_0$  is unreachable due to the finite time resolution of the observation. Direct comparison of  $D_i(t)$  and  $\tilde{D}_i(t)$  (SI Appendix, Fig. S4; also compare Fig. 3C and E) shows that the scaling law  $D_i(t), \tilde{D}_i(t) \propto |t - t_0|^{1/2}$  appears longer in the comoving frame than in the laboratory frame, indicating that the results in the comoving frame are more reliable. This will be supported in the next section on the basis of the director configuration around the disclination pair.

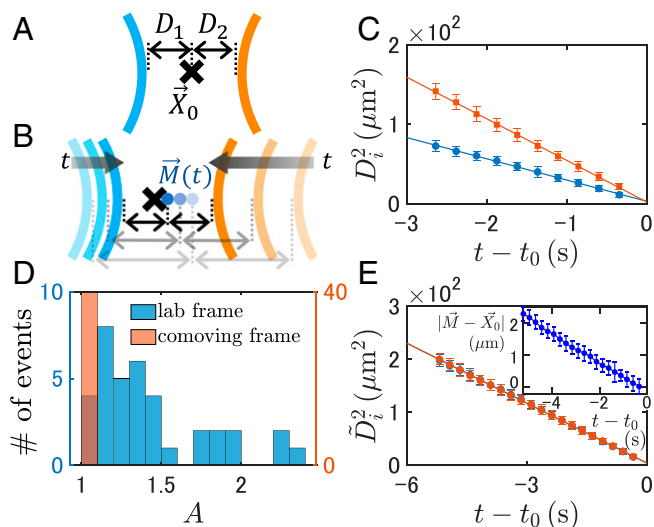


**Fig. 3.** Apparent asymmetry of in-plane reconnections. (A) Definition of the distances  $D_1(t)$  and  $D_2(t)$  from the reconnection point  $\vec{X}_0$ . (B) Sketch of the midpoint  $\vec{M}(t)$  of the points on the disclinations closest to the reconnection point  $\vec{X}_0$ . (C) Distance  $D_i(t)$  measured in the laboratory frame for an example pair of reconnecting disclinations. (D) Histograms of the asymmetry parameter  $A$  (the square root of the ratio of the two slopes in C; see text) measured in the laboratory frame (blue) and the comoving frame (red). Note that three outliers are not displayed in the blue histogram, taking  $A \approx 3.2$ ,  $A \approx 5.5$ , and  $A \approx 40$  in the laboratory frame, but in the comoving frame, all data, including those outliers, fell in the first bin ( $\max A = 1.03 \pm 0.01$ ). (E) Distance  $\tilde{D}_i(t)$  measured in the comoving frame for the pair shown in C. E, Inset shows the distance between the midpoint  $\vec{M}(t)$  and the reconnection point  $\vec{X}_0$  seen in the laboratory frame. The error bars in C and E indicate the uncertainty evaluated from the Gaussian fitting and the search for the reconnection point used here (Materials and Methods).

## Spontaneous Symmetry Restoring

We have found that the asymmetry present in the 2D pair annihilation of  $\pm 1/2$  point disclinations disappears for the in-plane reconnections of 3D disclination lines. Obviously, if two disclination lines were straight and had  $\pm 1/2$  director configurations around (Fig. 4A), this pair would exhibit the same asymmetry as its 2D counterpart. However, since  $+1/2$  and  $-1/2$  disclinations are homeomorphic in 3D (1, 2, 20), the director can actually take an intermediate configuration that continuously transforms between these two limiting structures (Fig. 4A). More precisely, the winding of the director around a disclination line is not characterized by the winding number but by a unit vector that specifies the rotation axis of the director, denoted by  $\vec{\Omega}$  (e.g., refs. 37 and 38). With the unit tangent vector  $\vec{t}$  whose head and tail are set arbitrarily, the director rotates right handed by  $180^\circ$  in the plane perpendicular to  $\vec{\Omega}$ , along a closed path that turns right handed about the tangent vector  $\vec{t}$ . If  $\vec{\Omega} = \vec{t}$  [or the angle  $\beta \equiv \cos^{-1}(\vec{\Omega} \cdot \vec{t}) = 0$ ], the director is essentially in the plane perpendicular to the disclination line, and the defect is equivalent to a  $+1/2$  point disclination in that plane. Similarly, if  $\vec{\Omega} = -\vec{t}$  ( $\beta = \pi$ ), it is equivalent to a  $-1/2$  point disclination. These two limiting structures, called the wedge disclinations, are interpolated continuously by intermediate  $\beta$ . In particular, if  $\vec{\Omega} \perp \vec{t}$  ( $\beta = \pi/2$ ), the director purely twists around the defect; hence, it is called a twist disclination.

Now, for a pair of reconnecting disclinations in plane, we have two tangent vectors  $\vec{t}_1$  and  $\vec{t}_2$ , which are parallel near the reconnection point, so that we choose  $\vec{t}_1 = \vec{t}_2$ . Then, it is reasonable to assume  $\vec{\Omega}_1 = -\vec{\Omega}_2$  ( $\beta_2 = \pi - \beta_1$ ) so that the disclinations may attract each other most effectively, as inferred from the disclination dynamics derived in the theoretical studies (37, 38). Indeed,

$\vec{\Omega}_1 = -\vec{\Omega}_2$  is expected in order to reduce the elastic energy cost due to the existence of the disclination pair. This leaves one free parameter,  $\beta_1$  (or  $\vec{\Omega}_1$ ). If  $\beta_1 = 0$  or  $\pi$ , we have a pair of  $\pm 1/2$  wedge disclinations (Fig. 4B, Upper), which is equivalent to a pair of annihilating point disclinations in 2D nematics and therefore, approaches asymmetrically (35, 39). By contrast, if  $\beta = \pi/2$ , we have a pair of twist disclinations (Fig. 4B, Lower) with  $\pi$  rotationally symmetric director field; in this case, the dynamics of the two disclinations should also be symmetric.

Our experimental results of the vanishing asymmetry suggest that all disclination pairs we observed spontaneously took the symmetric twist configurations. This can be attributed to the anisotropic elasticity of liquid crystal; bulk deformation of the director can be decomposed into splay, twist, and bend deformations, characterized by different elastic constants denoted by  $K_1$ ,  $K_2$ , and  $K_3$ , respectively (20). For the mesogen used here, MLC-2037, these are  $K_1 = 11.6$  pN,  $K_2 = 6.1 \pm 0.5$  pN,  $K_3 = 13.2$  pN (Materials and Methods and SI Appendix, Table S1). Similarly to other typical mesogens, the elastic constant for twist deformations is lower than that for splay and bend deformations. Then, it follows that the twist configuration of the disclination pair (Fig. 4B, Lower) is energetically favored over the wedge configuration (Fig. 4B, Upper), which involves splay and bend deformations of the director field. This explains why the twist configuration seemed to be exclusively observed in our experiments, accounting for the disappearance of the asymmetry.

Moreover, we confirm the realization of the twist configuration via the coefficient  $C$  of the power law in Eq. 1 as follows. Balancing the drag force  $J\gamma_1(\delta/2)$  according to Geurst et al. (40) with a dimensionless coefficient  $J \approx 1.9$ , the rotational viscosity  $\gamma_1$ , and the attractive force  $\pi K/2\delta$  exerted to the pair with  $\vec{\Omega}_1 = -\vec{\Omega}_2$  under the one-constant approximation  $K_1 = K_2 = K_3 \equiv K$  (37), we obtain

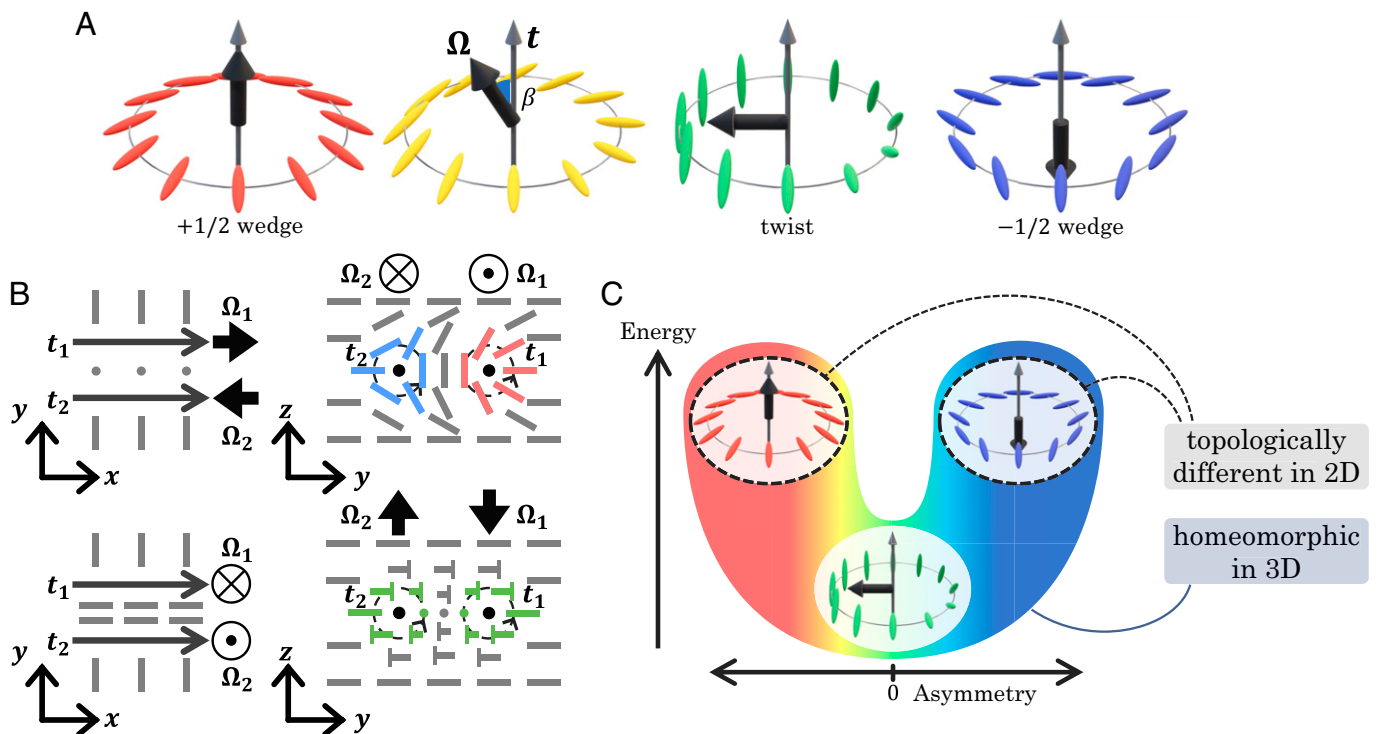


**Fig. 4.** Director configurations and asymmetry. (A) Director field around a disclination for different  $\vec{\Omega}$  (or  $\beta$ ). (B) Sketches of the director field around wedge (Upper) and twist (Lower) disclination pairs. The  $xy$  (Left) and  $yz$  (Right) cross-sections are shown. The “T” symbols indicate that the directors are not in the plane of the cross-section, with the T head above the paper. Note that the analyzed disclinations were not limited to those aligned in the  $x$  direction as sketched here. (C) Spontaneous symmetry restoring.

$$C^2 = \frac{2\pi K}{J\gamma_1}. \quad [3]$$

However, since the actual elastic constant is anisotropic, Eq. 3 is expected to hold with  $K \approx K_1, K_3$  for the wedge configuration and  $K \approx K_2$  for the twist one. From our data (Fig. 2) and  $\gamma_1 = 132 \text{ mPa} \cdot \text{s}$  for our mesogen (SI Appendix, Table S1), we obtain  $C^2 = 151 \pm 27 \mu\text{m}^2/\text{s}$  (the range of error being the SD), which is close to the value for the twist configuration,  $C^2 \approx 1.5 \times 10^2 \mu\text{m}^2/\text{s}$ , instead of that for the wedge one,  $C^2 \approx 3.1 \times 10^2 \mu\text{m}^2/\text{s}$ . This supports the realization of the twist configuration in the disclination pairs we observed as well as the resulting vanishing asymmetry we found in the comoving frame.

We also demonstrate the realization of the twist configuration in a more direct but destructive manner through the pattern of the electroconvection induced in the sample. It is known that nematic liquid crystal with negative dielectric anisotropy and positive conductivity anisotropy, such as the one used in the present work, shows roll convection under a moderate applied voltage (20). The direction of the rolls is determined by the director near the midplane; it is normal to the director if the director is parallel to the cell surfaces, while patches of rolls of different directions are formed if the director is perpendicular to the surfaces. Our observation reveals that the region between disclinations shows convection rolls normal to those in the outer region (SI Appendix, Fig. S5), indicating the twist director configuration as sketched in Fig. 4B, Lower (SI Appendix has details).

While the twist configuration is expected from the energy viewpoint, it is important to note that such a lowest-energy configuration is to describe the equilibrium state, while our observations deal with relaxation to it. Upon quenching from the turbulent state, we expect that there exist various types of disclinations, from wedge to twist and in between. However, since all these configurations are homeomorphic, disclinations are allowed to change the configurations continuously toward the lowest-energy state (i.e., the twist configuration). This is not possible for 2D nematics, for which  $+1/2$  and  $-1/2$  disclinations are topologically distinct. Mathematically, this is a consequence of the different homotopy groups between 2D and 3D nematics (1, 20). For 2D, it is  $\pi_1(\mathbb{R}P^1) = \mathbb{Z}$ , which distinguishes all different winding numbers. In contrast, its 3D counterpart is  $\pi_1(\mathbb{R}P^2) = \mathbb{Z}_2$ , which now distinguishes only the absence and the presence of a nontrivial defect configuration. In particular, wedge disclinations of winding number  $\pm 1/2$  are now identified through continuous transformation, with the symmetric twist state found in the middle at the lowest energy (Fig. 4C). This results in the realization of the symmetric reconnection dynamics, as we observed experimentally.

At this point, it is not difficult to generalize the argument. If the space of the order parameter field accommodating topological defects of interest is related to real space, such as the nematic case ( $\mathbb{R}P^{d-1}$  for  $d$ -dimensional space), the corresponding homotopy group may also depend on the dimensionality. In the case where there exist two asymmetric structures that are topologically distinct in a lower dimension but become homeomorphic in a higher dimension, such as the case of  $\pm 1/2$  nematic disclinations, the defect in the higher dimension is allowed to take an intermediate structure that continuously interpolates the two asymmetric analogs of those in the lower dimension. Then, it is likely that a symmetric intermediate structure exists. If it is energetically favored, the asymmetry present in the lower dimension will tend to disappear in the higher dimension spontaneously. In brief, if two topologically distinguished and asymmetric configurations in a lower dimension become homeomorphic in a higher dimension

and if the newly allowed symmetric configuration is energetically favorable, symmetry is spontaneously restored. The symmetry in the structure results in the symmetry in the dynamics. Our results on reconnecting nematic disclinations constitute a clear example of such spontaneous restoring of symmetry.

## Concluding Remarks

We carried out a direct confocal observation of disclination dynamics in 3D nematics using the accumulation of fluorescent dyes to disclinations. Our method successfully resolved characteristic dynamics of disclination lines, such as reconnections and loop shrinkage. Studying in-plane reconnection events in depth, we demonstrated the distance-time scaling law (Eq. 1) predicted for straight disclination pairs, despite the curved shape of the observed disclinations. Moreover, we revealed that the dynamics of reconnecting disclinations is only deceptively asymmetric in the 3D case, being actually symmetric in the comoving frame. This is explained by the spontaneous realization of symmetric twist configurations, which are energetically favored because of the lower twist elasticity. These observations led us to propose a mechanism of such spontaneous symmetry restoring from a general viewpoint of topology and energy. In this regard, it is important to investigate the generality and limitation of this concept in future studies. The first step would be to study intersecting reconnections. Although we restricted the analysis to in-plane reconnections in the present work, our argument suggests that the spontaneous symmetry restoring also holds for intersecting reconnections. Simulations in ref. 38 showed that at least the same scaling law holds for intersecting reconnections. Furthermore, it is of prominent importance to test the fate of the symmetry restoring in the case where the condition  $K_2 < K_1, K_3$  is not satisfied and consequently, the twist configuration does not correspond to the lowest-energy state. Such a situation may be realized by using the divergence of  $K_2$  near the nematic–smectic transition (20), by the drop of  $K_3$  near the transition to the twist–bend nematic phase (41), or by using nematic discotic liquid crystals (42).

Since the concept of topological defects is universal, it is important to think of similarities and dissimilarities in defect properties across different disciplines of physics. For example, quantum vortices in superfluid  $^4\text{He}$  are known to have similar interaction energy and show the same scaling law of  $\delta(t)$  (Eq. 1) as observed experimentally (6, 7, 36), while the corresponding homotopy group is different, and the rotation axis  $\vec{\Omega}$ , if defined analogously, is fixed to  $\vec{\Omega} = \vec{t}$  or  $-\vec{t}$ . Further, it is tempting to seek examples of the spontaneous symmetry restoring we proposed in this work. Disgratation of superfluid  $^3\text{He}$  is particularly interesting in this context, for which the homotopy group is  $\pi_1(SO(2)) = \mathbb{Z}$  for 2D and  $\pi_1(SO(3)) = \mathbb{Z}_2$  for 3D, and its asymmetric structures as well as energy have been thoroughly discussed (5). We hope that such approaches to general mechanisms will accelerate the multidisciplinary understanding of topological defects and that the visualization of nematic disclination dynamics reported here will be a useful tool in this line.

## Materials and Methods

**Sample Preparation and Defect Generation.** The experimental sample was prepared as follows for the main results on the in-plane reconnections, while changes for other experiments are described in the end of this subsection. The liquid crystal sample was nematic compound MLC-2037 (Merck; discontinued product) doped with 0.5 wt % tetra-*n*-butylammonium bromide and 0.005 wt % fluorescent dye Coumarin 545T. The mesogen MLC-2037 was chosen for its low birefringence  $\Delta n = 0.0649$  and negative dielectric anisotropy  $\Delta\epsilon < 0$

(SI Appendix, Table S1), the latter of which was used to induce electroconvection to generate disclinations (20). The sample was introduced to a handmade cell, which consists of a coverslip and a glass plate both coated with indium tin oxide and 130  $\mu\text{m}$ -thick polyimide tapes used as spacers. The inner surfaces were coated with polyvinyl alcohol and rubbed to realize a homogeneous planar alignment.

To study disclination dynamics, we generated a large density of disclinations by applying an alternating electric field (rms amplitude 150 V, frequency 50 Hz) to the sample, inducing an electrohydrodynamic turbulence called the dynamic scattering mode 2 (20, 43). Then, we removed the electric field and observed relaxation of disclinations by a confocal laser scanning microscope (Leica SP8; objective 20 $\times$ , numerical aperture 0.75, oil immersion) equipped with a resonant scanner working at 8 kHz and a piezo objective scanner. The fluorescent dyes were excited at 488 nm by laser light polarized in the direction perpendicular to the nematic easy axis, represented by  $x$  and  $y$  axes, respectively. The fluorescence signal in the range between 500 and 600 nm was confocally detected by a photomultiplier tube detector (pinhole size 20  $\mu\text{m}$ , roughly 0.35 times the Airy unit). The voxel size in the  $xy$  plane was 0.91  $\mu\text{m}$ , and the spacing between  $z$  slices was 1  $\mu\text{m}$ . The numbers of voxels were 512, 128, and 21 in the  $x$ ,  $y$ ,  $z$  directions, respectively. The time interval between consecutive confocal images was 0.255 s. Compared with this, the time needed for fluorescent dyes to follow the evolution of disclination lines is expected to be much shorter, which we evaluate to be roughly 1 ms, using a length scale 0.33  $\mu\text{m}$  reported as the apparent size of dye accumulation in ref. 29 and the typical value of the diffusion coefficient of dye molecules,  $10^{-10}$   $\text{m}^2/\text{s}$  (24, 30).

Below, we describe the experimental conditions used for other observations. Conditions and parameters that are not specified below were kept unchanged from those for the in-plane reconnections. The intersecting reconnection displayed in Fig. 1E was observed in a sample that contained 0.25 wt % tetra- $n$ -butylammonium bromide and 0.2 wt % Coumarin 545T. After an alternating voltage of rms amplitude 150 V and frequency 100 Hz was removed, we observed the intersecting reconnection in a manner similar to the case of the in-plane reconnections, except that the number of voxels was  $512 \times 64 \times 36$  and the time interval was 0.300 s. The loop shrinkage displayed in Fig. 1F was observed in a sample that contained 0.05 wt % tetra- $n$ -butylammonium bromide and 0.005 wt % Coumarin 545T.

**Image Analysis.** The data acquired by the confocal microscope were the fluorescence intensity detected at the 3D position  $(x, y, z)$  and time  $t$ . Using the 3D image at each time, we obtained cross-sections and extracted the coordinates of the disclinations as follows. First, we chose the cross-sections to use, either in the  $xz$  plane or in the  $yz$  plane, chosen so that the cross-sections become closer to perpendicular to the disclination lines. In each cross-section, the two disclinations appear as bright spots. These bright spots were fitted by a Gaussian function to obtain the coordinates of the spot centers. Repeating this over all cross-sections, we obtained a set of 3D coordinates along each disclination line. The closest distance  $\delta(t)$  between two disclinations (Fig. 2) was directly determined from these coordinates.

The time and the position of each reconnection event, as well as the distance  $D_i(t)$  ( $i = 1, 2$ ) of a disclination from the reconnection point, were determined as follows. For the reconnection time  $t_0$ , we determined it from the 2D image constructed from the transmitted excitation laser to benefit from the finer time resolution than that of the confocal images. For the position  $\vec{X}_0 = (X_0, Y_0, Z_0)$  of the reconnection point, we first approximately located it from the series of transmitted and confocal images ( $X_0$  and  $Y_0$  from the transmitted images,  $Z_0$  from the confocal images). Using this and the coordinates of the disclinations, we could evaluate the distance  $D_i(t)$  in the laboratory frame, but for the analysis presented in the paper, we evaluated  $D_i(t)$  more precisely in the following manner. First, we fitted the 3D coordinates of disclinations by smoothing splines to reduce the noise and to interpolate the lines appropriately. In general, smoothing splines  $s(x)$  for a dataset  $(x_i, y_i)$  is such a function that minimizes

$$p \sum_i w_i (y_i - s(x_i))^2 + (1 - p) \int \left( \frac{d^2 s}{dx^2} \right)^2 dx, \quad [4]$$

with a smoothing parameter  $p$  and a weight  $w_i$ , which is set to be one here. By adjusting  $p$ , we obtained smoothing splines that reproduced the defect shape

without high wave number components, for the two coordinates that spanned the cross-sections [i.e., for  $xz$  cross-sections, the obtained smoothing splines were  $x(y)$  and  $z(y)$ ]. Then, we also refined the estimate of the reconnection point  $\vec{X}_0$  by using the coordinates of the disclinations before the moment of the reconnection. Specifically, we determined  $\vec{X}_0$  in such a way that the scaling  $D_i(t) \simeq C_i |t - t_0|^{1/2}$  is satisfied most precisely in a time period before the reconnection under the constraint that  $\vec{X}_0$  is not changed by more than 3  $\mu\text{m}$  from the first rough estimate. This was done by evaluating  $D_i(t)$  for each candidate position  $\vec{X}_0$  in the range within 3  $\mu\text{m}$ , fitting it to  $D_i(t)^2 = a_i |t - t_0| + b_i$ , and choosing the candidate  $\vec{X}_0$  that minimizes  $b_1^2 + b_2^2$ . The distance  $\bar{D}_i(t)$  in the comoving frame was also determined analogously by using the position  $\vec{X}_0$  that drifts with the velocity of the comoving frame.

The errors in the estimates of  $\delta(t)$ ,  $D_i(t)$ ,  $\bar{D}_i(t)$  were evaluated as follows. For  $\delta(t)$ , the error bars in Fig. 2 indicate the square root of the sum of the squares of the uncertainties in all coordinates of the two closest points. For the coordinates in the cross-section, we used the 95% CI of the Gaussian fitting as the uncertainty; for the other coordinate, we used half the thickness of the cross-section (i.e., the voxel size) as the uncertainty. For  $D_i(t)$  and  $\bar{D}_i(t)$  (Fig. 3 C and E), the errors were evaluated from the uncertainties in the coordinates of the reconnection point and the closest point on the disclination line, again by the square root of the sum of the squares. The uncertainties in the coordinates of the reconnection point were considered to be half the size of the scanned region described above. For the uncertainties in the coordinates of the closest point on the disclination line, since the closest point was located on the smoothing spline, we only considered the uncertainties (95% CI) for the coordinates in the cross-section that is closest to the closest point on the spline.

**Estimation of  $K_2$ .** The twist elastic constant  $K_2$  of MLC-2037 was evaluated by using the Fréedericksz transition under an external magnetic field (20). The Fréedericksz transition point  $H_f^i$  corresponding to the elastic constant  $K_i$  is given by

$$H_f^i = \frac{\pi}{d} \sqrt{\frac{K_i}{\Delta\chi}}, \quad [5]$$

where  $d$  is the cell thickness and  $\Delta\chi$  is the magnetic anisotropy. For MLC-2037,  $\Delta\chi$  was unknown, but  $K_1$  is known (SI Appendix, Table S1). Therefore, we measured the Fréedericksz transition for both the splay and twist configurations, obtaining  $H_f^1$  and  $H_f^2$ , and used the ratio

$$\frac{H_f^2}{H_f^1} = \sqrt{\frac{K_2}{K_1}} \quad [6]$$

to determine  $K_2$  from  $K_1$ .

We used a ready-made cell with homogeneous planar alignment (EHC, KSRO-25/B107M6NTS;  $d = 25$   $\mu\text{m}$ ) filled with MLC-2037. Using a superconducting magnet, we applied a magnetic field that was perpendicular to the cell surface for the splay configuration and parallel to the cell surface but that was perpendicular to the easy axis for the twist configuration. The Fréedericksz transition point was determined by measuring the retardation change through the transmitted light intensity that changed in a swept magnetic flux density  $B$  under crossed Nicols (SI Appendix, Fig. S6). The measurement for the twist configuration was performed at oblique incidence ( $5^\circ$ ) to reduce the effect of polarization rotation (44, 45).

We measured the Fréedericksz transition eight times for the splay configuration and three times for the twist configuration. The light source was either a halogen lamp or a light-emitting diode. For each measurement, we determined the transition point twice: when the magnetic field was increased and decreased. As a result, we obtained a total of 16 estimates of the transition point  $B_1^i$  and 6 estimates of  $B_2^i$ . By using all of them, we determined our final estimates at  $B_1^i = 4.4 \pm 0.1$  T and  $B_2^i = 3.2 \pm 0.1$  T. Then, it follows, by using Eq. 6 and  $K_1 = 11.6$  pN (SI Appendix, Table S1), that  $K_2 = 6.1 \pm 0.5$  pN.

**Data, Materials, and Code Availability.** Analysis results have been deposited in figshare (<https://doi.org/10.6084/m9.figshare.21130301>) (46).

**ACKNOWLEDGMENTS.** We thank F. Araoka at RIKEN Center for Emergent Matter Science (CEMS) (Japan) for providing the experimental setup for the

determination of  $K_2$  and for his help to measure that of MLC-2037; M. Tsubota for his suggestion to study the coefficient  $C$  of Eq. 1; M. Kobayashi for drawing our attention to disgyration; and G. Tóth, C. Denniston, and J. M. Yeomans for allowing us to use and analyze their data in ref. 39. We acknowledge the material data of MLC-2037 in *SI Appendix, Table S1* provided by Merck and their permission to present them in this work. We also thank C. Denniston, J.-i. Fukuda, O. Ishikawa, T. Ohzono, K. Katoh, J. V. Selinger, R. L. B. Selinger, and H. Watanabe for useful

discussions. This work was supported in part by Japan Science and Technology Agency (JST) Precursory Research for Embryonic Science and Technology (PRESTO) Grant JPMJPR18L6; by KAKENHI from Japan Society for the Promotion of Science Grants JP19H05800, JP19H05144, JP20H01826, and JP22J12144; by a JSR Fellowship (The University of Tokyo); and by the Forefront Physics and Mathematics Program to Drive Transformation (FoPM), a World-leading Innovative Graduate Study (WINGS) Program (The University of Tokyo).

1. M. Nakahara, *Geometry, Topology and Physics* (Taylor & Francis, Boca Raton, FL, 2nd ed., 2003).
2. P. M. Chaikin, T. C. Lubensky, *Principles of Condensed Matter Physics* (Cambridge University Press, Cambridge, United Kingdom, 2000).
3. A. Vilenkin, E. P. S. Shellard, *Cosmic Strings and Other Topological Defects* (Cambridge University Press, Cambridge, United Kingdom, revised ed., 2000).
4. W. Zurek, Cosmological experiments in condensed matter systems. *Phys. Rep.* **276**, 177–221 (1996).
5. D. Vollhardt, P. Wölfle, *The Superfluid Phases of Helium 3* (Dover, New York, NY, 2013).
6. G. P. Bewley, M. S. Paoletti, K. R. Sreenivasan, D. P. Lathrop, Characterization of reconnecting vortices in superfluid helium. *Proc. Natl. Acad. Sci. U.S.A.* **105**, 13707–13710 (2008).
7. E. Fonda, D. P. Meichle, N. T. Ouellette, S. Hormoz, D. P. Lathrop, Direct observation of Kelvin waves excited by quantized vortex reconnection. *Proc. Natl. Acad. Sci. U.S.A.* **111** (suppl. 1), 4707–4710 (2014).
8. Y. Minowa *et al.*, Visualization of quantized vortex reconnection enabled by laser ablation. *Sci. Adv.* **8**, eabn1143 (2022).
9. S. Serafini *et al.*, Vortex reconstructions and rebounds in trapped atomic bose-einstein condensates. *Phys. Rev. X* **7**, 021031 (2017).
10. T. B. Saw *et al.*, Topological defects in epithelia govern cell death and extrusion. *Nature* **544**, 212–216 (2017).
11. K. Kawaguchi, R. Kageyama, M. Sano, Topological defects control collective dynamics in neural progenitor cell cultures. *Nature* **545**, 327–331 (2017).
12. A. Doostmohammadi, J. Ignés-Mullol, J. M. Yeomans, F. Sagués, Active nematics. *Nat. Commun.* **9**, 3246 (2018).
13. S. Čopar, J. Aplinc, Ž. Kos, S. Žumer, M. Ravnik, Topology of three-dimensional active nematic turbulence confined to droplets. *Phys. Rev. X* **9**, 031051 (2019).
14. J. Binysh, Ž. Kos, S. Čopar, M. Ravnik, G. P. Alexander, Three-dimensional active defect loops. *Phys. Rev. Lett.* **124**, 088001 (2020).
15. G. Duclos *et al.*, Topological structure and dynamics of three-dimensional active nematics. *Science* **367**, 1120–1124 (2020).
16. K. Copenhagen, R. Alert, N. S. Wingreen, J. W. Shaevitz, Topological defects promote layer formation in *myxococcus xanthus* colonies. *Nat. Phys.* **17**, 211–215 (2021).
17. Y. Maroudas-Sacks *et al.*, Topological defects in the nematic order of actin fibres as organization centres of *Hydra* morphogenesis. *Nat. Phys.* **17**, 251–259 (2021).
18. L. J. Ruske, J. M. Yeomans, Morphology of active deformable 3D droplets. *Phys. Rev. X* **11**, 021001 (2021).
19. T. Shimaya, K. A. Takeuchi, Tilt-induced polar order and topological defects in growing bacterial populations. arXiv [Preprint] (2022). <https://arxiv.org/abs/2106.10954v3> (Accessed 19 July 2022).
20. P. G. de Gennes, J. Prost, *The Physics of Liquid Crystals* (International Series of Monographs on Physics, Oxford University Press, New York, NY, 2nd ed., 1995), vol. 83.
21. I. Chuang, R. Durrer, N. Turok, B. Yurke, Cosmology in the laboratory: Defect dynamics in liquid crystals. *Science* **251**, 1336–1342 (1991).
22. X. Wang, D. S. Miller, E. Bukusoglu, J. J. de Pablo, N. L. Abbott, Topological defects in liquid crystals as templates for molecular self-assembly. *Nat. Mater.* **15**, 106–112 (2016).
23. I. Smalyukh, S. Shiyonovskii, O. Lavrentovich, Three-dimensional imaging of orientational order by fluorescence confocal polarizing microscopy. *Chem. Phys. Lett.* **336**, 88–96 (2001).
24. O. D. Lavrentovich, Fluorescence confocal polarizing microscopy: Three-dimensional imaging of the director. *Pramana J. Phys.* **61**, 373–384 (2003).
25. T. Lee, R. P. Trivedi, I. I. Smalyukh, Multimodal nonlinear optical polarizing microscopy of long-range molecular order in liquid crystals. *Opt. Lett.* **35**, 3447–3449 (2010).
26. R. P. Trivedi, I. I. Klevets, B. Senyuk, T. Lee, I. I. Smalyukh, Reconfigurable interactions and three-dimensional patterning of colloidal particles and defects in lamellar soft media. *Proc. Natl. Acad. Sci. U.S.A.* **109**, 4744–4749 (2012).
27. P. J. Ackerman, I. I. Smalyukh, Reversal of helicoidal twist handedness near point defects of confined chiral liquid crystals. *Phys. Rev. E* **93**, 052702 (2016).
28. J. S. Evans, P. J. Ackerman, D. J. Broer, J. van de Lagemaat, I. I. Smalyukh, Optical generation, templating, and polymerization of three-dimensional arrays of liquid-crystal defects decorated by plasmonic nanoparticles. *Phys. Rev. E Stat. Nonlin. Soft Matter Phys.* **87**, 032503 (2013).
29. T. Ohzono, K. Katoh, J. I. Fukuda, Fluorescence microscopy reveals molecular localisation at line defects in nematic liquid crystals. *Sci. Rep.* **6**, 36477 (2016).
30. L. Blinov, V. Chigrinov, *Electrooptic Effects in Liquid Crystal Materials, Partially Ordered Systems* (Springer-Verlag, 1994).
31. B. Yurke, A. N. Pargellis, I. Chuang, N. Turok, Coarsening dynamics in nematic liquid crystals. *Phys. B* **178**, 56–72 (1992).
32. I. Chuang, B. Yurke, A. N. Pargellis, N. Turok, Coarsening dynamics in uniaxial nematic liquid crystals. *Phys. Rev. E Stat. Phys. Plasmas Fluids Relat. Interdiscip. Topics* **47**, 3343–3356 (1993).
33. P. T. Mather, D. S. Pearson, R. G. Larson, Flow patterns and disclination-density measurements in sheared nematic liquid crystals I: Flow-aligning 5CB. *Liq. Cryst.* **20**, 527–538 (1996).
34. T. Ishikawa, O. D. Lavrentovich, Crossing of disclinations in nematic slabs. *Eur. Lett.* **41**, 171–176 (1998).
35. D. Svenšek, S. Žumer, Hydrodynamics of pair-annihilating disclination lines in nematic liquid crystals. *Phys. Rev. E Stat. Nonlin. Soft Matter Phys.* **66**, 021712 (2002).
36. C. Denniston, Disclination dynamics in nematic liquid crystals. *Phys. Rev. B Condens. Matter* **54**, 6272–6275 (1996).
37. C. Long, X. Tang, R. L. B. Selinger, J. V. Selinger, Geometry and mechanics of disclination lines in 3D nematic liquid crystals. *Soft Matter* **17**, 2265–2278 (2021).
38. C. D. Schimming, J. Viñals, Singularity identification for the characterization of topology, geometry, and motion of nematic disclination lines. *Soft Matter* **18**, 2234–2244 (2022).
39. G. Tóth, C. Denniston, J. M. Yeomans, Hydrodynamics of topological defects in nematic liquid crystals. *Phys. Rev. Lett.* **88**, 105504 (2002).
40. J. Geurst, A. Spruijt, C. Gerritsma, Dynamics of  $s = 1/2$  disclinations in twisted nematics. *J. Phys. (Paris)* **36**, 653–664 (1975).
41. K. Adlem *et al.*, Chemically induced twist-bend nematic liquid crystals, liquid crystal dimers, and negative elastic constants. *Phys. Rev. E Stat. Nonlin. Soft Matter Phys.* **88**, 022503 (2013).
42. M. Osipov, S. Hess, The elastic constants of nematic and nematic discotic liquid crystals with perfect local orientational order. *Mol. Phys.* **78**, 1191–1201 (1993).
43. S. Kai, W. Zimmermann, Pattern dynamics in the electrohydrodynamics of nematic liquid crystals. *Prog. Theor. Phys. Suppl.* **99**, 458–492 (1989).
44. S. Chandrasekhar, *Liquid Crystals* (Cambridge University Press, Cambridge, United Kingdom, 2nd ed., 1993).
45. P. P. Karat, "Electric and magnetic field effects in liquid crystals," PhD thesis, Mysore University, Mysore, India (1977).
46. Y. Zushi, K. A. Takeuchi, Dataset for "Scaling and Spontaneous Symmetry Restoring in Reconnecting Nematic Disclinations." figshare. [https://figshare.com/articles/dataset/dataset\\_for\\_Y.Zushi\\_and\\_K.A.Takeuchi\\_Scaling\\_and\\_Spontaneous\\_Symmetry\\_Restoring\\_in\\_Reconnecting\\_Nematic\\_Disclinations/21130301](https://figshare.com/articles/dataset/dataset_for_Y.Zushi_and_K.A.Takeuchi_Scaling_and_Spontaneous_Symmetry_Restoring_in_Reconnecting_Nematic_Disclinations/21130301). Deposited 19 September 2022.